OPTICA

High-speed two-photon microscopy with adaptive line-excitation

Yunyang Li,[1] Shu Guo,[1] Ben Mattison,[2,3] Junjie Hu,[1] Kwun Nok Mimi Man,[4,5] and Weijian Yang[1,3,*]

[1]Department of Electrical and Computer Engineering, University of California, Davis, California 95616, USA
[2]Department of Biomedical Engineering, University of California, Davis, California 95616, USA
[3]Biomedical Engineering Graduate Group, University of California, Davis, California 95616, USA
[4]Department of Biochemistry and Molecular Medicine, University of California, Davis, California 95616, USA
[5]Current address: Max Planck Florida Institute for Neuroscience, Jupiter, Florida 33458, USA
*wejyang@ucdavis.edu

Received 13 May 2024; revised 24 June 2024; accepted 1 July 2024; published 15 August 2024

We present a two-photon fluorescence microscope designed for high-speed imaging of neural activity at cellular resolution. Our microscope uses an adaptive sampling scheme with line illumination. Instead of building images pixel by pixel via scanning a diffraction-limited spot across the sample, our scheme only illuminates the regions of interest (i.e., neuronal cell bodies) and samples a large area of them in a single measurement. Such a scheme significantly increases the imaging speed and reduces the overall laser power on the brain tissue. Using this approach, we performed high-speed imaging of the neuronal activity in mouse cortex *in vivo*. Our method provides a sampling strategy in laser-scanning two-photon microscopy and will be powerful for high-throughput imaging of neural activity.

https://doi.org/10.1364/OPTICA.529930

1. INTRODUCTION

Two-photon laser scanning microscopy can image deep into the tissue with a high signal-to-background ratio, tight axial confinement, and low phototoxicity [1–3]. When used in conjunction with functional fluorescent indicators, two-photon microscopy provides a powerful tool to monitor neuronal signals and activity [4–7]. Conventional two-photon microscopes build the image by raster scanning a laser focus point by point on the sample, resulting in a tradeoff between sampling speed, spatial resolution, and field of view (FOV). When imaging a sample with a large FOV at fine spatial resolution, the temporal resolution could become poor, which may not faithfully capture the neuronal signals. The single-beam scanning strategy thus limits the imaging throughput. Another limitation of conventional two-photon microscopes is the blind scanning strategy. In particular, it is highly inefficient to record dynamic signals where the sample is repeatedly imaged in time. It not only wastes time imaging areas without useful information, but it also deposits unnecessary heat and induces possible damage to the sample.

Various types of beam multiplexing techniques [8–16] have been proposed and demonstrated to alleviate the tradeoff between the spatiotemporal resolution and FOV and to increase the imaging throughput. In these approaches, multiple beams are used to image the sample, each scanning a sub-FOV. The signals are then demixed and assigned to the proper pixels in the whole image. While effective, the imaging throughput is still limited by the number of beams that can be multiplexed and the demixing quality. Furthermore, as the imaging throughput increases, the overall laser power on the tissue will inevitably increase. This induces excessive heat on the brain tissue and can cause tissue damage [17].

Random-access two-photon microscopes realized by acousto-optic deflectors (AODs) [18–20] can overcome the limitations of blind scanning strategies and reduce heating of the brain tissue. Instead of raster scanning, AODs rapidly steer the beam in the imaging process to select the desirable regions of interest (ROIs), such as the neuronal cell bodies. We term this type of sampling strategy adaptive sampling, as the sampling location is tailored to the ROIs on the tissue. While AODs have an increased imaging speed and reduced photodamage on the tissue, they are generally expensive, sensitive to excitation wavelength, and have a limited scanning angle and thus FOV. Another strategy for adaptive sampling utilizes raster scanning with a temporally modulated laser source [21]. However, it is incompatible with beam multiplexing schemes and has a limited imaging throughput.

We report a new adaptive sampling strategy for two-photon microscopes with high imaging speed/throughput and low laser power on the brain tissue. This microscope is optimized for population calcium imaging, where the ROIs are the neuronal cell bodies. Instead of using a diffracted-limited spot, we image the sample by scanning a short excitation line. Furthermore, we spatially modulate the line pattern so only the neuronal cell bodies are excited. Our scheme significantly increases the imaging speed as it images a large portion of the tissue in a single measurement and thus reduces the total amount of measurements per frame. The

imaging process itself pre-processes the data otherwise recorded by the point scanning approach, as it sums up the pixels within the short-excitation line, which mostly belong to a single ROI. The number of pixels in the recording is considerably reduced, which could reduce the storage and alleviate the demand for the required computational resources to process the data (i.e., segmentation and temporal traces demixing and extraction). Finally, by only illuminating the ROIs, it noticeably reduces the laser power on the tissue. Using this microscope, we performed high-speed calcium imaging of mouse cortex *in vivo*. Compared to the typical two-photon microscope using the point scanning strategy, we increased the imaging speed by $\sim 5-10\times$ and reduced the laser power on the brain by $>10\times$. Our new adaptive sampling strategy is compatible with beam multiplexing techniques and holds great promise to significantly enhance the imaging throughput capabilities of two-photon microscopy.

2. PRINCIPLE OF ADAPTIVE LINE-EXCITATION

In our adaptive sampling scheme, the brain tissue is illuminated with a short line that is dynamically patterned to match the local structure of the ROIs. Scanning such a spatially modulated excitation line over the tissue allows us to capture the ROIs but not the background area in the image plane [Figs. 1(a)–1(c)]. The spatial modulation of the excitation line is realized by a digital micromirror device (DMD), which has been widely used to shape the illumination beams through its intensity modulation or indirect phase modulation via a Lee hologram [22] in two-photon systems, for applications in imaging [23–25], micro-fabrication [26], and optogenetics [27]. Here, the DMD functions as an intensity modulator and is loaded with a binary mask that matches the morphology of the neuronal cell bodies (i.e., ROIs) on the sample plane. The binary mask contains the spatial footprint of the ROIs, obtained through a calibration process where we image the sample plane in high resolution, followed by segmentation. The DMD is placed at a conjugate plane of the sample plane. We shape the laser beam (femtosecond laser at 920 nm) into a line and scan it across the DMD through a resonant scanner (8 kHz) and galvanometer mirror. The deflected light from the DMD is then spatially modulated to carry the pertinent information of the ROIs, which is optically relayed to the sample plane to image the brain tissue [Fig. 1(d), Supplement 1, Notes 1–2]. The pattern on the DMD is obtained by a calibration process, which performs a high-resolution recording of the sample, equivalent to the point-by-point scanning scheme. This can be conducted in the same microscope by merely configuring the DMD pattern so the ON pixels form periodic rows (Supplement 1, Note 3, Supplement 1, Figs. S3–S4), without any physical change of the optical system. This ensures an optimal alignment and calibration for pattern registration in adaptive illumination.

In addition to spatial light modulator, the DMD also serves as a diffraction grating, which could create the temporal focusing effect [28–33] and thus tighten the axial confinement of the point-spread function on the sample plane (Supplement 1, Note 4, Supplement 1, Fig. S7). The DMD is configured to be at blazed condition and positioned such that the chief ray (corresponding to the central wavelength of the laser light) of the diffraction beam at the blazed condition propagates on axis to the subsequent optics after the DMD (Supplement 1, Note 2, Supplement 1, Fig. S1). As a result, the DMD surface is not parallel with the scan lens but is tilted to fulfill the blazed angle condition. In this way, the spatial focusing plane of the scan lens is mismatched with the temporal focusing plane (i.e., the DMD surface) while the beam is being scanned. To resolve this, we deliberately introduced an in-plane decentering spatial displacement of the scan lens [34] (Supplement 1, Note 2, Supplement 1, Fig. S2). This ensures the overlap of the spatial focusing plane and temporal focusing plane and a consistent pattern of the incident line illumination across the entire surface of the DMD.

Compared to the conventional point-by-point blind sampling scheme, our method has two distinct features. First, we sample a larger region in a single measurement. This reduces the number of rows in the imaging and thus increases the frame rate. In our demonstration, we shaped the excitation line to be $\sim$11.5 μm in length ($1/e^2$) on the sample plane [Fig. 1(e)], which is similar to the diameter of the neuronal cell body in a mouse brain (10–15 μm). This allows a fast imaging speed while maintaining cellular resolution and avoiding excessive signal crosstalk between adjacent neurons in a single measurement, as most of the measurements would contain information about only a single neuron in a typical labeling condition. Furthermore, our method effectively pre-processes the images otherwise recorded by the blind sampling approach, as we condense the pixels, which mostly belong to a single source, to a single pixel. This not only saves the memory to store the raw images but also reduces the data volume and, thus, the computation time in the subsequent data processing (segmentation and extraction of the temporal activity traces). Signal demixing could be processed post hoc, with prior knowledge of all the source locations. This could resolve the signal crosstalk in the scenarios when a single measurement contains information from more than one source. Second, the beam modulation from the DMD enables an exclusive sampling of the neuronal cell bodies and avoids the unnecessary excitation of background regions. It greatly reduces the overall laser power delivered to the brain tissue and, thus, the thermal damage. Though our excitation pattern was a line, it was thin ($\sim$2.0 μm, full-width-at-half-maximum, FWHM) [Fig. 1(e)]. The axial FWHM of the PSF was measured to be $\sim$16.5 μm [Fig. 1(f)].

3. RESULTS

A. Simulations of the Adaptive Line-Excitation Sampling Process in Neuronal Imaging

We simulated the adaptive line-excitation sampling process in a simulated calcium imaging dataset and investigated whether the signal from individual neurons, including those having spatial overlap with each other, could be faithfully extracted (Fig. 2, Supplement 1, Fig. S8). We generated a simulated calcium recording [Fig. 2(a), 500 μm × 500 μm, 500 × 500 pixels, 2000 frames] [35] with GCaMP6f at 15 Hz frame rate, with 80% Poisson noise and 80% Gaussian noise added. We generated a binary mask from the spatial footprint of the neurons [Fig. 2(b)] and created the adaptive-line sampled videos from a bi-directional scanning trajectory on the original high-resolution recording. We then used CaImAn, a constrained non-negative matrix factorization (CNMF) algorithm [36,37], with the prior knowledge of the neuronal locations from the binary mask, to extract the neuronal spatial footprint [Fig. 2(c)] and temporal activity traces [Fig. 2(d)] in the adaptive-line sampled recording. Though the number of pixels in individual neurons in the adaptive-line sampled recordings is small, CaImAn successfully segmented the spatial footprint

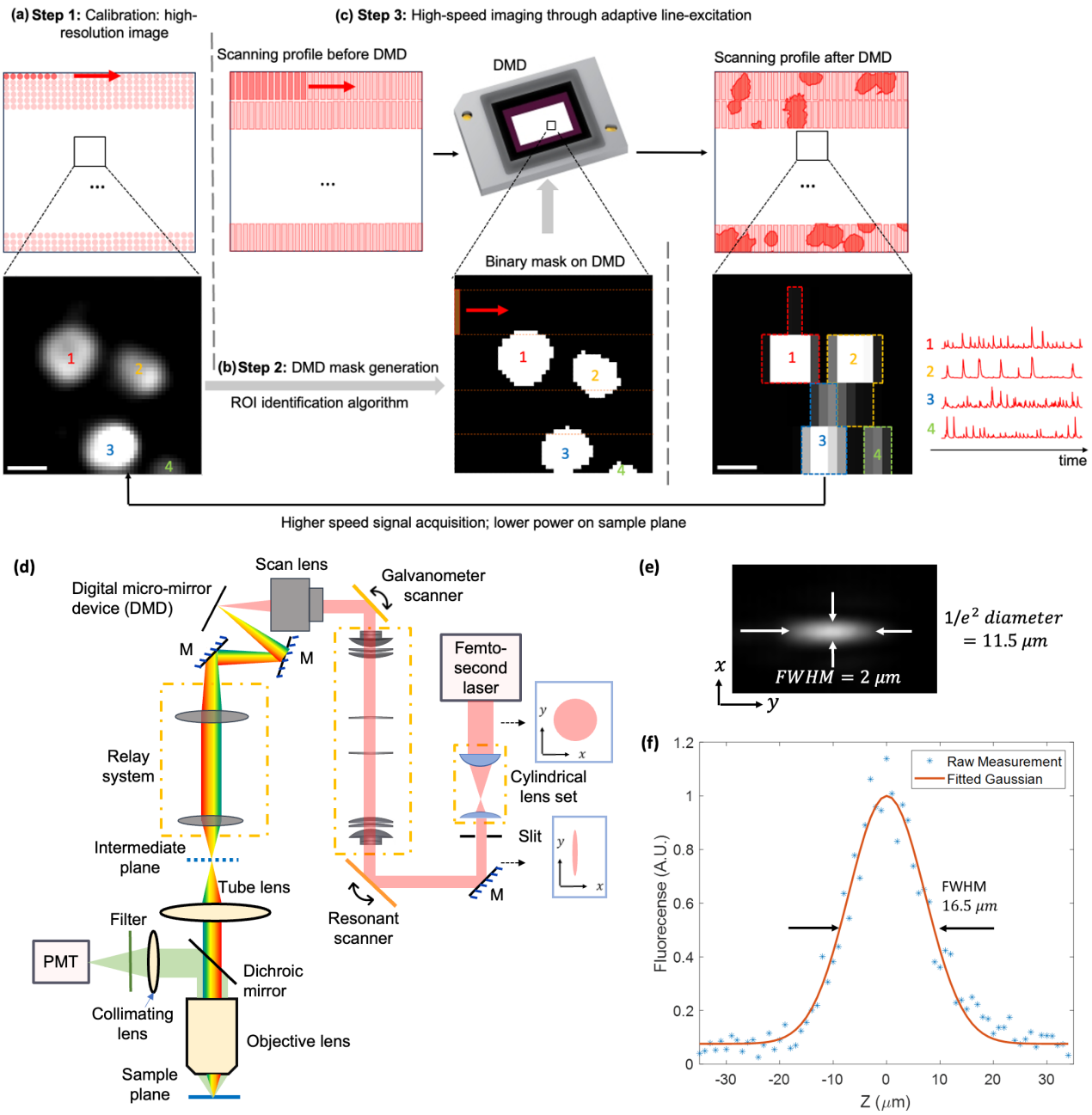

Fig. 1. Principle, optical setup, and point-spread function (PSF) of the two-photon scanning microscope with adaptive line-excitation. (a)–(c) Working principles of adaptive line-excitation. (a) A high-resolution video of the neuronal activity is acquired in the calibration step through an equivalent point scanning strategy. (b) The ROIs (i.e., neuronal cell bodies) could then be segmented. They are then binarized into a mask and loaded to the DMD. The laser (920 nm femtosecond laser) light is first shaped to a short line and incident to the DMD, which is located at the conjugate plane of the sample plane and works as an intensity spatial modulator. (c) The beam diffracted from the DMD carries the information of the ROI, and illuminates the corresponding part of the sample ROI. Only the ROIs but not the background region are imaged. Top, illustration of the excitation scheme on the sample, with the arrow showing the beam scanning direction. Bottom, (a)(c) zoom-in view of a sub-region of the image recorded by the photomultiplier tube (PMT). (b) Binary mask loaded on the DMD. The four ROIs are labeled in different numbers. (d) Schematic of the two-photon microscope setup with adaptive line-excitation scheme. The laser beam is first shaped into a short line, which is scanned by a resonant scanner and a galvanometer mirror onto the DMD. Light diffracted from the DMD is relayed to the sample plane through a relay system and the tube lens and objective lens. The fluorescence is detected by the PMT. M, mirror. (e) Measured PSF in the lateral direction (xy) for line-excitation. (f) Measured axial PSF using 5 μm fluorescent beads. Scale bar in (a) and (c) is 10 μm.

of the neurons with a high intersection over union (IoU) values against the reference spatial footprint calculated from the binary mask and scanning trajectory [Fig. 2(e)] and extracted the temporal traces with high Pearson correlation coefficients (PCCs) against the ground truth [Fig. 2(f)]. Crucially, the neuronal signals could be generally demixed from neurons with overlapping spatial footprints [Fig. 2(g)]. There are a small portion of ROIs that cannot be demixed well due to their strong spatial overlap or weak signal-to-noise ratio in the non-overlap regions, which is a general challenge of CNMF (Supplement 1, Fig. S8). We note that both

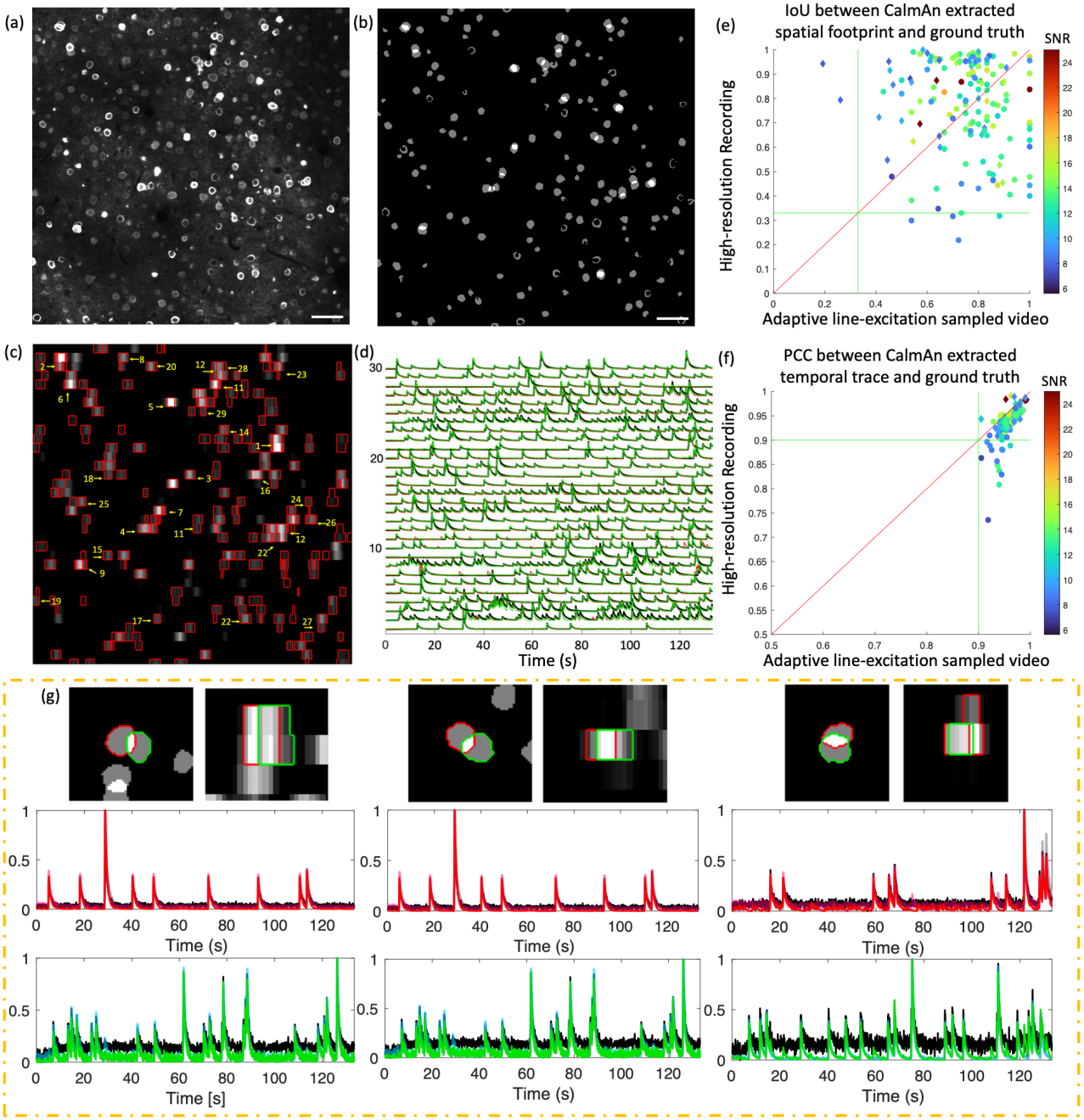

Fig. 2. Simulation of the adaptive line-excitation sampling in calcium imaging. (a) Time-series standard-derivation projection frame of the simulated high-resolution calcium imaging video. (b) Mask for (a) showing individual ROIs, constructed from the ground truth in simulation. Some of the neurons have spatial overlaps with others. (c) Time-series average projection frame of the video constructed by the adaptive line-excitation sampling on the original high-resolution video, using the mask shown in (b). The frame was resized to the same dimension as the original video. The spatial footprints of the extracted ROIs through CalmAn are outlined in red. (d) Extracted normalized temporal activity traces of the representative neurons in (c), which were indicated by the yellow arrows in (c). Black, ground truth with noise and background included; green, extracted traces using CalmAn on the original high-resolution video; red, extracted traces using CalmAn on the adaptive line-excitation sampled video. (e) Intersection over union (IoU) between the CalmAn-extracted spatial footprint and the ground truth of individual neurons in the high-resolution video versus that calculated for the adaptive line-excitation sampled video. The green lines are indications of IoU = 0.33. The color of each dot shows the signal-to-noise ratio (SNR) of individual neurons in the original high-resolution video. The SNR is defined as the maximum of the denoised temporal signal (with signal baseline included) over the standard deviation of the noise. The ROIs with spatial overlap with others are indicated by diamond shape symbols, while the isolated ROIs are plotted in circular dots. (f) Same as (e), but for the Pearson correlation coefficient (PCC) between the CalmAn-extracted traces and the noise-free ground truth traces. The green lines are indications of PCC = 0.9. (g) Three pairs of comparisons illustrating that the neuronal signals from the neurons with spatial overlaps could be demixed in the adaptive line-excitation sampled video. In each pair group, the top-left and top-right figures show the spatial footprint of the neurons in the high-resolution ground truth and the time-series average projection frame of adaptive line-excitation sampled video, respectively. The middle panel shows the temporal traces of the ROI contoured in red: gray, ground truth without noise and background; black, ground truth with noise and background included; red, CalmAn-extracted from the adaptive line-excitation sampled video; magenta, CalmAn-extracted from the high-resolution video. Similarly, the bottom panel shows the temporal traces of ROI contoured in green: gray, ground truth without noise and background; black, ground truth with noise and background included; green, CalmAn-extracted from the adaptive line-excitation sampled video; cyan, CalmAn-extracted from the high-resolution video. All the traces are normalized to [0,1]. Scale bar in (a) and (b) is 50 μm.

the IoU and the PCC values in the adaptive-line sampled recording do not differ significantly from the CalmAn results on the original high-resolution recording ($p = 0.32$ for IoU, $p = 0.54$ for PCC, paired t-test). Overall, our results illustrated that the adaptive-line sampled recording, though significantly down-sampled in one direction, preserved the information as the original high-resolution recording and could be processed through calcium imaging processing tools such as CalmAn, and with significantly reduced computational resources because of the reduced number of pixels in the video.

B. Validation of Adaptive Illumination Through Phantom Samples

We validated the beam patterning capability of the DMD and the concept of adaptive sampling through fluorescent phantom samples (Fig. 3). Using a uniform fluorescent slab, we first assessed the encoding capabilities of our system in defining arbitrary binary masks and projecting the desired patterns onto the sample plane [Figs. 3(a) and 3(b)]. The image recorded by the PMT matched well with the binary mask loaded on the DMD, confirming the conjugate relationship between the DMD and sample plane. We then validated that the binary pattern on the DMD, when projected to the sample, could indeed overlap with the ROIs on the sample structures [Figs. 3(c)–3(f)]. Here, we used a phantom sample composed of randomly distributed fluorescent beads with a diameter of 12 μm. Through a calibration process that is equivalent to point scanning (Supplement 1, Note 3, Supplement 1, Figs. S3–S4), we obtained a high-resolution image of the sample with 256 × 320 pixels, in a resolution of ∼2.0 μm × 2.2 μm [Fig. 3(c)]. Such a calibration process mapped individual DMD pixels to the sample coordinates. We then transformed the high-resolution image to the DMD mask [Fig. 3(d)] and performed the high-speed line scanning with adaptive sampling. The acquired image matched well with the DMD mask, verifying that the mask aligned well with the sample plane [Fig. 3(e)]. Finally, we simulated the high-speed scanning results based on the high-resolution image [Fig. 3(c)] and the bi-directional scanning trajectory. The simulated image [Fig. 3(f)] is highly similar to the experimental result [Fig. 3(e)], further verifying the robust mapping relationship between the DMD and the sample structure.

C. High-Speed Calcium Imaging of Neuronal Activity In Vivo

We conducted *in vivo* experiments to monitor the cortical activity of layer 2/3 in the primary visual cortex (V1) in an awake mouse transfected with calcium indicators GCaMP6f [38] (Supplement 1, Note 7), over an FOV of ∼500 μm × 695 μm. Following the procedure outlined in Figs. 1(a)–1(c), we first

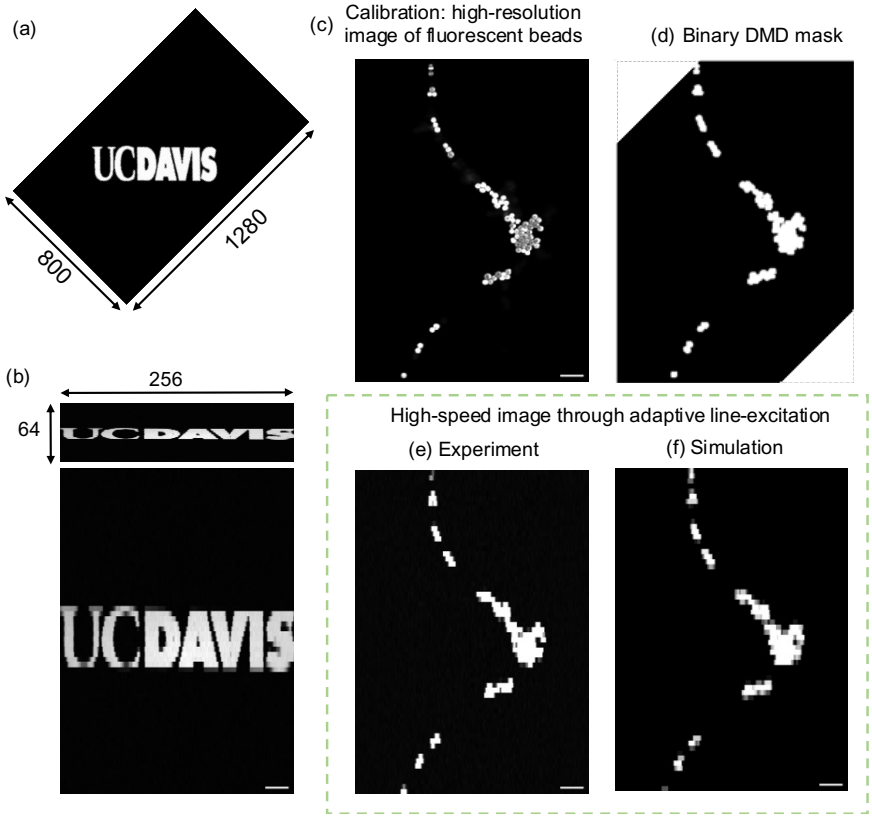

Fig. 3. Validation of the adaptive sampling scheme through phantom samples. (a),(b) Projection of the DMD mask onto a uniform fluorescent slab through adaptive short-line excitation. (a) DMD mask (1280 × 800 pixels) with characters "UC DAVIS." (b) Top: raw image (256 × 64 pixels) acquired from PMT through adaptive line-excitation with bi-directional scanning; bottom: interpolated and resized image (500 × 695 pixels) with square pixels. (c)–(f) Imaging of a phantom sample with randomly distributed fluorescent beads, in 12 μm diameters. (c) A high-resolution image of the sample was acquired through the equivalent point scanning approach. (d) Binary mask on the DMD. The two corner regions of the mask were outside the DMD active regions and were not displayed. (e) Single frame of the recording from the sample acquired at 198 Hz, using the adaptive line-excitation with bi-directional scanning. (f) Simulated high-speed image based on the binary mask and the bi-directional scanning trajectory of the resonant scanner. Scale bar in (b),(c),(e),(f) is 50 μm.

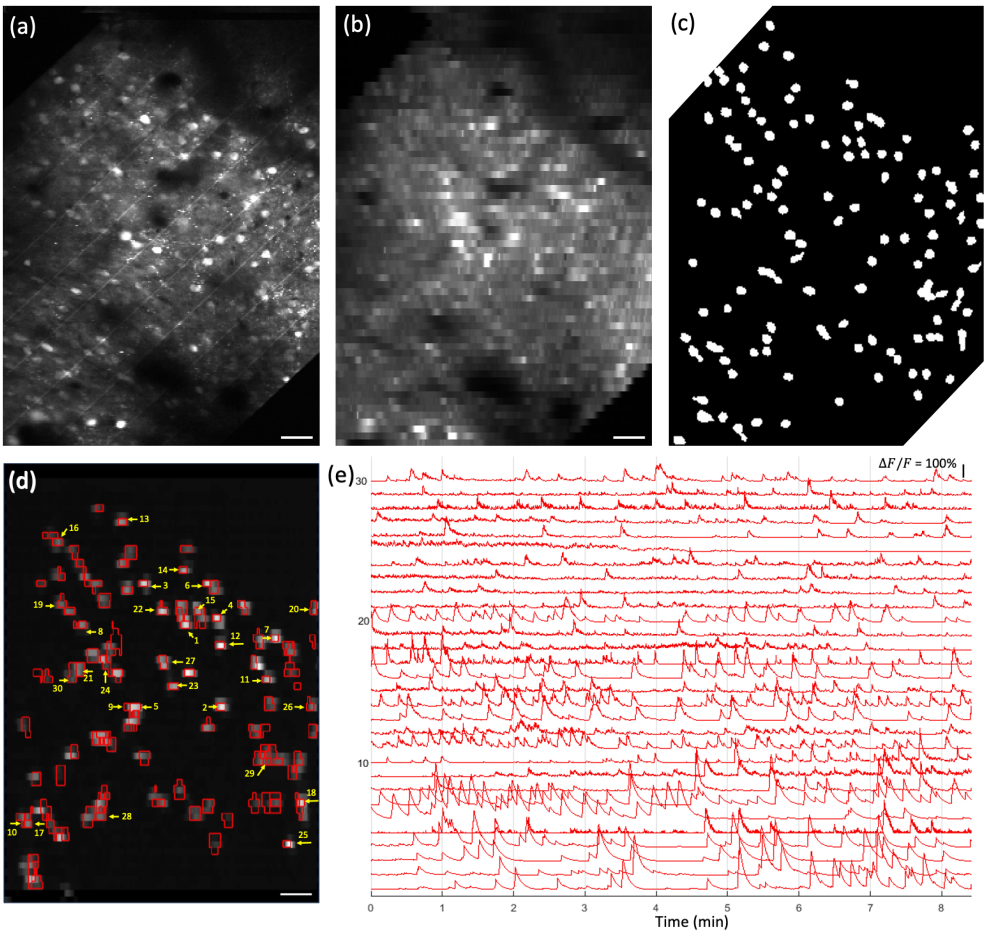

Fig. 4. *In vivo* calcium imaging of mouse V1 at 150 μm depth using the adaptive line-excitation two-photon microscope. (a) Time-series average projection frame of the high-resolution image from the effective point scanning method, which includes the fine contours of the neurons and the background. The image has 256 × 320 pixels over a 500 μm × 695 μm FOV. The periodic lines were artifacts and formed due to the tilted scanning trajectory and corresponding shifted DMD pixels (Supplement 1, Note 3, Supplement 1, Fig. S6). They did not impact the segmentation results. (b) Time-series average projection frame of the line-scanning sampled video (256 × 64 pixels) for the same FOV in (a) without adaptive sampling, where all the pixels in the DMD were turned on. (c) Corresponding binary mask for (a), constructed from the ROI segmentation algorithm of SUNS. (d) Time-series average projection frame of the line-scanning sampled video (256 × 64 pixels) with adaptive sampling, by applying the mask on DMD. Only the ROIs defined in (c) were illuminated and sampled. The spatial footprints of the extracted ROIs through CalmAn are outlined in red. (e) Temporal activity traces of the representative neurons recorded at 198 Hz, which were indicated by the yellow arrows in (d). The temporal activity traces were extracted by CalmAn. Scale bar in (a),(b),(d) is 50 μm.

calibrated the spatial location of the ROIs by obtaining the high-resolution recording of the sample plane [Fig. 4(a), 256 × 320 pixels, in a resolution of 2.0 μm × 2.2 μm] at a depth of 150 μm and segmenting the recording using SUNS [39] [Fig. 4(c), Supplement 1, Note 6], a state-of-the-art fast segmentation algorithm on calcium imaging. In the represented example, we found 130 ROIs, which were the active neurons during the video acquisition period in calibration (∼5 min, Supplement 1, Note 3). With the spatial footprints of these ROIs displayed on the DMD, we conducted high-speed recording through adaptive line-excitation [Fig. 4(d), 256 × 64 pixels]. Notably, our sampling strategy reduced the number of rows scanned by the resonant scanner and thus increased the frame rate. With the height of each row being ∼11 μm, and using a bi-directional scanning scheme, we achieved a frame rate of 198 Hz over the FOV ∼500 μm × 695 μm. Such a frame rate is significantly higher than the typical ones in conventional two-photon microscopes using the point scanning strategy. Compared to the case where only line-excitation was used but without the adaptive sampling strategy [Fig. 4(b), with the binary mask on the DMD being all "1" by turning on all DMD pixels], the adaptively sampled images [Fig. 4(d)] used a significantly smaller average laser power on sample (∼14× smaller than the case without adaptive sampling, as the occupied area of ROIs over the entire plane is ∼7.25%). In our case of adaptive line-excitation, only ∼1.5 mW of average laser power was delivered to the brain tissue, which was a considerable drop to avoid thermal damage to the mouse brain. The non-ROI background regions appear to be dark in Fig. 4(d) as they were not imaged, which could facilitate the subsequent ROI segmentation and temporal trace extraction. Finally, from the high-speed recording with the adaptive line-excitation strategy, we extracted the temporal activity traces of individual ROIs through CalmAn [36,37] [Fig. 4(e)]. In the CalmAn processing, as we had prior knowledge of the pixel locations of individual ROIs, we used their centroid pixels to initialize the search for their spatial footprint (Supplement 1, Note 6). This increased the efficiency and efficacy of the algorithm. We further validated the

system's capabilities by imaging the cortex at a depth of 450 μm, where we successfully extracted 91 ROIs (Supplement 1, Fig. S5).

4. DISCUSSION

In summary, we proposed and demonstrated the concept of adaptive sampling with line illumination in two-photon microscopy. The DMD functions as an amplitude spatial light modulator as well as a blazed grating for temporal focusing. By using line illumination and only exciting the regions of interest rather than the entire field of view, we could achieve a high imaging speed (up to 198 Hz with 500 μm × 695 μm FOV) while reducing the overall laser power and thus phototoxicity on the sample. Crucially, our method is compatible with many other beam multiplexing techniques, such as spatiotemporal multiplexing [9,14], so as to further increase the imaging throughput. The capability to reject the illumination on the non-ROI background regions becomes particularly important to reduce the overall laser power and heat generation in the brain tissue when multiple beams scan the tissue. While designed for high-speed imaging, our microscope retains the capability for the equivalent point scanning high-resolution imaging by properly setting and cycling the DMD pattern in synchronization with the scanner and without physically modifying the optical setup, as in our calibration step. Our adaptive sampling microscope setup could be further optimized, as the current PSF (axial FWHM–16.5 μm) may result in out-of-focus backgrounds when imaging the neuronal cell bodies. Such a background could be eliminated by further tightening the axial extent of the beam (Supplement 1, Note 4). Alternatively, the background signals near the cell bodies could be captured by a proper configuration of the DMD mask. Algorithms such as matrix factorization could then be used to remove the local background from the cell bodies.

The line-scanning approach is one type of PSF engineering used to increase imaging throughput [40]. Here, we used short-line excitation with a single-pixel detector. Two similar strategies involve pairing a long-line excitation with a camera [41] or a long-line excitation with a linear PMT array [42]. They have challenges in imaging deep due to light scattering. Two other long-line-excitation strategies use a single pixel detector and require imaging the sample through multiple line patterns and then reconstructing the image computationally through principles of compressive sensing [43] or topographical imaging [44]. They typically require intense computational resources or complex system setups. Our strategy avoids these challenges. One advantage of our method is that the signal in each measurement over the short-line illumination mostly comes from the same neuronal source. Such a strategy essentially pre-processes the data, and thus reduces the signal processing time as the number of pixels in the image is reduced. If there are multiple sources in a single short line, they could be separated through demixing algorithms such as non-negative matrix factorization (e.g., CaImAn [36,37]). We note that our selective excitation method shares a similar concept with SLAP2 [45,46]. There, instead of using a short-line to perform a two-dimensional raster scanning across the DMD, SLAP2 uses a long-line to scan the DMD in one dimension. If there are multiple ROIs along the line, only pixels for a specific ROI are turned on in the DMD at a time to avoid imaging multiple ROIs together and mixing their signals. The mask of the DMD could then be changed upon the next scan to image another ROI. When the ROIs are highly sparse, the frame rate could be particularly high. However, the effective insertion loss at the DMD is significantly high, necessitating the use of a high-power laser. In our approach, the length of the line is designed to be comparable to the diameter of the neurons. This results in a substantially reduced effective insertion loss at the DMD and allows one to use a typical 80 MHz femtosecond laser, which is more commonly available and cost-effective.

Previous reports have demonstrated block-scanning [31,32], where the illumination was a 5 μm × 5 μm block, and their fluorescence was summed together into a single measurement. There, a low-repetition-rate laser was used, and each block was sampled with one laser pulse, so as to avoid oversampling in the fast-scanning axis. The resonant scanner had to synchronize with the laser pulse clock, which required a custom-tuned resonant scanner and complicated electronic controls. Our method uses line illumination, and the linewidth in the fast-scanning axis is thin. Hence, we could use a typical 80 MHz laser without synchronization between the scanner and the laser clock. Furthermore, as the line rate is determined by the resonant frequency of the scanner, short-line scanning could achieve the same speed as block scanning.

Our adaptive sampling strategy uses a DMD to spatially modulate the excitation pattern. Compared to existing adaptive sampling approaches (AODs [18–20] and adaptive laser source [21]), our method requires simpler hardware and is compatible with beam multiplexing. In particular, in contrast to the method using a temporally modulated laser source, we do not need the synchronization of the modulator and the scanner. Like other adaptive sampling approaches, our method requires prior knowledge of the ROIs, and the imaging quality is sensitive to the motion of the tissue. This could be readily resolved by including a real-time feedback loop and compensating the motion through additional scanners [20].

In typical two-photon microscopes, there is a tradeoff between imaging throughput and required laser power on the tissue. Our adaptive line-excitation two-photon microscope alleviates this tradeoff and could simultaneously increase the imaging throughput and reduce the on-tissue laser power. By combining our method with beam multiplexing techniques and using a faster resonant scanner, the imaging speed could be in kilohertz and thus suitable for voltage imaging. Though not demonstrated here, our method is also compatible with three-dimensional/volumetric imaging by incorporating an axial scanning mechanism (such as tunable lenses) after the DMD. This allows for calcium imaging over a large 3D volume. Finally, while we focused on imaging neuronal cell bodies here, we could also optimize our method (i.e., by increasing the numerical aperture of the beam so as to reduce the width and axial extent of the excitation line) to image ROIs with finer features such as dendrites and spines.

Funding. Burroughs Wellcome Fund (CASI 1015761); National Science Foundation (CAREER 1847141); National Institute of Neurological Disorders and Stroke (R01NS118289); National Eye Institute (R01NS118289) .

Acknowledgment. We acknowledge Dr. Kangning Zhang for fruitful discussions on calcium imaging data processing and Dr. Lin Tian for providing the surgical setup and tools for mice surgery.

Disclosures. The authors declare no conflicts of interest.

Data availability. Data underlying the results presented in this paper are not publicly available at this time but may be obtained from the authors upon reasonable request.

Supplemental document. See Supplement 1 for supporting content.

REFERENCES

1. W. Denk, J. H. Strickler, and W. W. Webb, "Two-photon laser scanning fluorescence microscopy," Science **248**, 73–76 (1990).
2. W. R. Zipfel, R. M. Williams, and W. W. Webb, "Nonlinear magic: multiphoton microscopy in the biosciences," Nat. Biotechnol. **21**, 1369–1377 (2003).
3. F. Helmchen and W. Denk, "Deep tissue two-photon microscopy," Nat. Methods **2**, 932–940 (2005).
4. R. Yuste and W. Denk, "Dendritic spines as basic functional units of neuronal integration," Nature **375**, 682–684 (1995).
5. C. Stosiek, O. Garaschuk, K. Holthoff, *et al.*, "*In vivo* two-photon calcium imaging of neuronal networks," Proc. Natl. Acad. Sci. USA **100**, 7319–7324 (2003).
6. K. Svoboda and R. Yasuda, "Principles of two-photon excitation microscopy and its applications to neuroscience," Neuron **50**, 823–839 (2006).
7. C. Grienberger and A. Konnerth, "Imaging calcium in neurons," Neuron **73**, 862–885 (2012).
8. K. H. Kim, C. Buehler, K. Bahlmann, *et al.*, "Multifocal multiphoton microscopy based on multianode photomultiplier tubes," Opt. Express **15**, 11658–11678 (2007).
9. A. Cheng, J. T. Goncalves, P. Golshani, *et al.*, "Simultaneous two-photon calcium imaging at different depths with spatiotemporal multiplexing," Nat. Methods **8**, 139–142 (2011).
10. P. Mahou, M. Zimmerley, K. Loulier, *et al.*, "Multicolor two-photon tissue imaging by wavelength mixing," Nat. Methods **9**, 815–818 (2012).
11. W. Yang, J. E. Miller, L. Carrillo-Reid, *et al.*, "Simultaneous multi-plane imaging of neural circuits," Neuron **89**, 269–284 (2016).
12. S. Han, W. Yang, and R. Yuste, "Two-color volumetric imaging of neuronal activity of cortical columns," Cell Rep. **27**, 2229–2240 (2019).
13. D. R. Beaulieu, I. G. Davison, K. Kilic, *et al.*, "Simultaneous multiplane imaging with reverberation two-photon microscopy," Nat. Methods **17**, 283–286 (2020).
14. J. Wu, Y. Liang, S. Chen, *et al.*, "Kilohertz two-photon fluorescence microscopy imaging of neural activity *in vivo*," Nat. Methods **17**, 287–290 (2020).
15. J. Demas, J. Manley, F. Tejera, *et al.*, "High-speed, cortex-wide volumetric recording of neuroactivity at cellular resolution using light beads microscopy," Nat. Methods **18**, 1103–1111 (2021).
16. J. Platisa, X. Ye, A. M. Ahrens, *et al.*, "High-speed low-light *in vivo* two-photon voltage imaging of large neuronal populations," Nat. Methods **20**, 1095–1103 (2023).
17. K. Podgorski and G. Ranganathan, "Brain heating induced by near-infrared lasers during multiphoton microscopy," J. Neurophysiol. **116**, 1012–1023 (2016).
18. B. F. Grewe, D. Langer, H. Kasper, *et al.*, "High-speed *in vivo* calcium imaging reveals neuronal network activity with near-millisecond precision," Nat. Methods **7**, 399–405 (2010).
19. G. Katona, G. Szalay, P. Maak, *et al.*, "Fast two-photon *in vivo* imaging with three-dimensional random-access scanning in large tissue volumes," Nat. Methods **9**, 201–208 (2012).
20. V. A. Griffiths, A. M. Valera, J. Y. Lau, *et al.*, "Real-time 3D movement correction for two-photon imaging in behaving animals," Nat. Methods **17**, 741–748 (2020).
21. B. Li, C. Wu, M. Wang, *et al.*, "An adaptive excitation source for high-speed multiphoton microscopy," Nat. Methods **17**, 163–166 (2020).
22. W. H. Lee, "Binary synthetic holograms," Appl. Opt. **13**, 1677–1682 (1974).
23. M. Ren, J. Chen, D. Chen, *et al.*, "Aberration-free 3D imaging via DMD-based two-photon microscopy and sensorless adaptive optics," Opt. Lett. **45**, 2656–2659 (2020).
24. N. Wijethilake, M. Anandakumar, C. Zheng, *et al.*, "DEEP-squared: deep learning powered de-scattering with excitation patterning," Light Sci. Appl. **12**, 228 (2023).
25. Y. D. Sie, C.-Y. Chang, C.-Y. Lin, *et al.*, "Fast and improved bioimaging via temporal focusing multiphoton excitation microscopy with binary digital-micromirror-device holography," J. Biomed. Opt. **23**, 116502 (2018).
26. P. Somers, Z. Liang, J. E. Johnson, *et al.*, "Rapid, continuous projection multi-photon 3D printing enabled by spatiotemporal focusing of femtosecond pulses," Light Sci. Appl. **10**, 199 (2021).
27. M. Brunstein, J. Lubetzki, C. Moutoussamy, *et al.*, "Fast 2-photon stimulation using holographic patterns," Opt. Express **31**, 39222–39238 (2023).
28. D. Oron, E. Tal, and Y. Silberberg, "Scanningless depth-resolved microscopy," Opt. Express **13**, 1468–1476 (2005).
29. G. Zhu, J. van Howe, M. Durst, *et al.*, "Simultaneous spatial and temporal focusing of femtosecond pulses," Opt. Express **13**, 2153–2159 (2005).
30. E. Papagiakoumou, V. de Sars, V. Emiliani, *et al.*, "Temporal focusing with spatially modulated excitation," Opt. Express **17**, 5391–5401 (2009).
31. R. Prevedel, A. J. Verhoef, A. J. Pernia-Andrade, *et al.*, "Fast volumetric calcium imaging across multiple cortical layers using sculpted light," Nat. Methods **13**, 1021–1028 (2016).
32. S. Weisenburger, F. Tejera, J. Demas, *et al.*, "Volumetric Ca^{2+} imaging in the mouse brain using hybrid multiplexed sculpted light microscopy," Cell **177**, 1050–1066 (2019).
33. E. Papagiakoumou, E. Ronzitti, and V. Emiliani, "Scanless two-photon excitation with temporal focusing," Nat. Methods **17**, 571–581 (2020).
34. T. Chakraborty, B. Chen, S. Daetwyler, *et al.*, "Converting lateral scanning into axial focusing to speed up three-dimensional microscopy," Light Sci. Appl. **9**, 165 (2020).
35. A. Song, J. L. Gauthier, J. W. Pillow, *et al.*, "Neural anatomy and optical microscopy (NAOMi) simulation for evaluating calcium imaging methods," J. Neurosci. Methods **358**, 109173 (2021).
36. E. A. Pnevmatikakis, D. Soudry, Y. Gao, *et al.*, "Simultaneous denoising, deconvolution, and demixing of calcium imaging data," Neuron **89**, 285–299 (2016).
37. A. Giovannucci, J. Friedrich, P. Gunn, *et al.*, "CaImAn an open source tool for scalable calcium imaging data analysis," Elife **8**, e38173 (2019).
38. T. W. Chen, T. J. Wardill, Y. Sun, *et al.*, "Ultrasensitive fluorescent proteins for imaging neuronal activity," Nature **499**, 295–300 (2013).
39. Y. J. Bao, S. Soltanian-Zadeh, S. Farsiu, *et al.*, "Segmentation of neurons from fluorescence calcium recordings beyond real time," Nat. Mach. Intell. **3**, 590 (2021).
40. W. Yang and R. Yuste, "*In vivo* imaging of neural activity," Nat. Methods **14**, 349–359 (2017).
41. H. Dana, A. Marom, S. Paluch, *et al.*, "Hybrid multiphoton volumetric functional imaging of large-scale bioengineered neuronal networks," Nat. Commun. **5**, 3997 (2014).
42. S. Murphy, N. Watson, P. Zhao, *et al.*, "Design and Characterization of Two-Photon Line Excitation Array Detection (2p-LEAD) Microscopy for Monitoring In Vivo Neuronal Activity," Proc. SPIE, High-Speed Biomedical Imaging and Spectroscopy VIII **12390**, 1239006 (2023).
43. M. Alemohammad, J. Shin, J. R. Stroud, *et al.*, "High-speed compressive line-scanned two photon microscopy," in *Biophotonics Congress: Biomedical Optics* (2020), paper BTu1C.3.
44. A. Kazemipour, O. Novak, D. Flickinger, *et al.*, "Kilohertz frame-rate two-photon tomography," Nat. Methods **16**, 778–786 (2019).
45. K. Podgorski and M. Xie, "Recording neurons' synaptic input patterns with scanned line projection microscopy," https://www.mbfbioscience.com/wp-content/uploads/2023/12/SLAP2-Poster-1.pdf.
46. G. Jaindl and J. R. Glaser, "Scanned line angular projection two photon laser scanning (SLAP2) microscopy for real-time (kilohertz rates) volumetric in vivo imaging at subcellular resolution," https://www.mbfbioscience.com/wp-content/uploads/2023/07/SLAP2_Research-Poster.pdf.

Supplemental Document

High-speed two-photon microscopy with adaptive line-excitation: supplement

YUNYANG LI,[1] SHU GUO,[1] BEN MATTISON,[2,3] JUNJIE HU,[1] KWUN NOK MIMI MAN,[4,5] AND WEIJIAN YANG[1,3,*]

[1] *Department of Electrical and Computer Engineering, University of California, Davis, California 95616, USA*
[2] *Department of Biomedical Engineering, University of California, Davis, California 95616, USA*
[3] *Biomedical Engineering Graduate Group, University of California, Davis, California 95616, USA*
[4] *Department of Biochemistry and Molecular Medicine, University of California, Davis, California 95616, USA*
[5] *Current address: Max Planck Florida Institute for Neuroscience, Jupiter, Florida 33458, USA*
[*] *wejyang@ucdavis.edu*

Supplement DOI: https://doi.org/10.6084/m9.figshare.26139925

Parent Article DOI: https://doi.org/10.1364/OPTICA.529930

High-speed two-photon microscopy with adaptive line-excitation

YUNYANG LI[1], SHU GUO[1], BEN MATTISON[2,3], JUNJIE HU[1], KWUN NOK MIMI MAN[4,5], AND WEIJIAN YANG[1,3,*]

[1]*Department of Electrical and Computer Engineering, University of California, Davis, Davis, CA 95616, USA*
[2]*Department of Biomedical Engineering, University of California, Davis, Davis, CA 95616, USA*
[3]*Biomedical Engineering Graduate Group, University of California, Davis, Davis, CA 95616, USA*
[4]*Department of Biochemistry and Molecular Medicine, University of California, Davis, Davis, CA 95616, USA*
[5]*Current address: Max Planck Florida Institute for Neuroscience, Jupiter, FL 33458, USA*
*****wejyang@ucdavis.edu*

Supplementary Information

Supplementary Note

1. System setup of the two-photon microscopy with adaptive line-excitation

We home-built the two-photon microscope with the adaptive line-excitation scheme (Fig. 1(d)) based on an Olympus open-stand frame. The system utilizes an 80 MHz repetition rate femtosecond laser (Axon 920-2, Coherent Inc.), which has intrinsic pulse compensation and power adjustment components, producing a 920 nm-centered excitation wavelength. The beam first goes through a cylindrical lens set and a slit with adjustable width (VA100CP, Thorlabs), so its spatial profile is shaped to be a line shape. The beam is then scanned by a resonant scanner mirror (4×5 mm^2 size, SC-30, Electro-Optical Products Corp) and a galvanometer scanner (GVS001, Thorlabs). The two scanners are conjugated to each other through a set of relay lenses adopted from ref [1]. After a scan lens [1], the beam is focused and scanned on the DMD (DLP650LNIR, Texas Instruments), which is placed at the back focal plane of the scan lens to ensure its conjugate relationship with the sample plane. After the DMD, the beam goes through a 4f relay system (Thorlabs, AC-508-150-B and AC-508-180-AB), followed by a tube lens (TTL200MP2, Thorlabs) and a water-immersion objective lens (CFI75 LWD 16X, Nikon). The effective magnification between the DMD plane and the sample plane is 13.3×. The excitation beam, whose pattern is dynamically modulated by the DMD as it scans, is then focused on the sample plane.

In the collection path, the fluorescent emission passes through the same objective lens, is reflected at the dichroic mirror (FF705-Di01-25x36, Semrock), and finally reaches the PMT (H7422-40, Hamamatsu) after a GFP bandpass filter (FF03-525/50-25, Semrock) and short-pass filter (FF01-715/SP-25, Semrock). The current signal from the PMT is then converted to voltage signal through a transimpedance amplifier (TIA60, Thorlabs), before being collected by a high-speed data acquisition card (vDAQ, Vidrio Technologies). ScanImage [2] is used to control the entire system.

The lateral excitation profile of the illumination beam was characterized by imaging the exciting pattern on a uniform fluorescent slab through a camera after the slab, in a transmission configuration. The axial excitation profile of the illumination beam was characterized by taking a z-stack of a 5 μm fluorescent bead sample through a translation stage (OptiScan III, Prior).

2. Configuration of the DMD in the optical system

The DMD used in our setup has 1280×800 pixels over an active region of 13.824×8.64 mm^2. The DMD can reach a frame rate with 1-bit binary at 10.752 kHz with a development kit (SuperSpeed .65" WXGA, ViALUX). The "ON" and "OFF" states are tilted $\pm 12°$ with respect to the DMD surface. It can be used as a diffraction grating [3] with a 10.59° blazed angle at 920 nm wavelength. In our system, the DMD surface is rotated by 45° along the incident beam so that the incidence beam and the diffraction beam at blazed condition are on a plane parallel to the optical table (Supplementary Fig. S1). The DMD is tilted such that the chief ray (corresponding to the central wavelength of the laser light) of the diffraction beam at the blazed condition propagates on the axis to the subsequent optics after the DMD. The diffraction light with orders other than the order of blazed condition is filtered out before the subsequent optical components after the DMD.

To ensure the spatial focal plane of the scan lens overlaps with the temporal focal plane (i.e., the DMD surface) while the beam is being scanned, we deliberately introduced an in-plane decentering spatial displacement of the scan lens [4] (Supplementary Fig. S2). This introduces an aberration that compensates for the mismatch between the spatial focusing plane and the temporal focusing plane, thereby ensuring a consistent pattern of the incident line illumination across the entire surface of the DMD with a high Strehl ratio [Supplementary Fig. S2(d)].

Instead of shifting the scan lens, a wedge prism could be utilized to accommodate the spatial focusing plane on the DMD surface [5]. This strategy requires both the incident beam and the modulated diffracted beam from the DMD pass through the wedge prism. Therefore, it requires additional optical elements other than the prism (e.g. polarization beam splitter and optical waveplate) and a fine alignment of the DMD tilting angle. Compared with this method, our method is simpler, while maintaining a good PSF and Strehl ratio across the field of view [Supplementary Fig. S2(d)].

3. System calibration and the generation of the high-resolution image

The adaptive sampling process begins with a calibration to acquire the high-resolution structural image of the sample. Such a calibration could be conducted by operating the microscope in an equivalent point-scanning mode (Supplementary Fig. S3-S4). There, we designed a set of five DMD masks, each being a periodic line pattern, i.e., two out of ten lines are turned on. The lines turned on are shifted by two lines in the next pattern. Thus, in the first DMD mask, lines numbered 1, 2, 11, 12, 21, 22, and so forth are turned to "ON" state, while the remaining lines are set to "OFF". In the second DMD mask, lines numbered 3, 4, 13, 14, 23, 24, and so on are turned to "ON" state. This process continues until the fifth DMD mask, where lines numbered 9, 10, 19, 20, 29, 30, and so forth are turned to "ON" state. For each DMD mask, we scan the laser light in the same line-shape across the DMD and acquire an image through the PMT. Effectively, the illumination pattern becomes a spot on the sample (~$1.95 \times 2.17\ \mu m^2$). Through a sequential combination of the rows of the five PMT images, we could obtain one high-resolution image, equivalent to point-scanning. By cycling the five DMD masks continuously, we could record the high-resolution video in an effective frame rate of ~21.6 Hz.

As the intensity along the excitation line is not strictly uniform, we introduce offsets for the start of the scanning position of the galvanometer mirror for each of the five DMD masks, so the center of the line illumination always overlaps with the lines that are turned as "ON" state from the each DMD mask (Supplementary Fig. S4). This ensures the illumination intensity of each spot on the high-resolution image is the same. Such a process is realized by MROI functionality in ScanImage. When the high-resolution image acquisition starts, the MROI scheme shifts the starting position of each FOV by adjusting the offset voltage, corresponding to a 2-line shift at the DMD plane. Meanwhile, an external trigger signal is sent from vDAQ to

the DMD, which synchronizes the DMD pattern display with MROI shifting under the driven mode.

In the experimental high-resolution image (Fig. 4(a) and Supplementary Fig. S5(a)), there appear periodic line patterns. These are artifacts originated from the exact scanning trajectory of the beam, which is illustrated in Supplementary Fig. S6. Ideally, the excitation line scans along the fast-scanning axis horizontally without any tilting (upper image in Supplementary Fig. S6(a)). In practice, the scanning trajectory is tilted along the slow scanning axis (lower image in Supplementary Fig. S6(a)). Since we acquired the high-resolution image by mimicking the point scanning strategy, the turned-on pixels on the DMD should be aligned with the exact scanning trajectory. However, such a perfect matching between the scanning trajectory and the turned-on pixels on the DMD requires continuously spatial modulation, which is impossible for pixelized DMD. We apply periodic pixel shifts on the DMD to modulate the turned-on pixels, as a 'tilted line' (Supplementary Fig. S6(b)). As a result, the center area of line illumination could always be projected to the sample plane, maintaining optimal power efficiency. Meanwhile, because of the discrete nature of DMD pixels, there will be more overlapping between the line illumination and the DMD's turned-on pixels at the junctions of each shift. This results in a higher laser power delivery on the sample, thus forming periodic lines in the high-resolution image (Supplementary Fig. S6(c)). The pixel-shifting position is defined according to the tilting of the scanning trajectory, and the actual distribution of periodic lines could change for different experiment setups.

4. Axial resolution of the short-line PSF and temporal focusing

The short-line PSF used in this work could be characterized by two excitation NAs, one in X, and one in Y which are referred to as the high NA (X) and low NA (Y) directions. The expected axial profiles for different short lines were simulated using Fourier optics (Supplementary Fig. S7). Here, our high and low NAs are characterized by the $1/e^2$ extent of the Gaussian beam measured before the scan lens (thus before DMD and therefore before any temporal focusing effect by the DMD) and scaled to the back aperture of our objective lens by a magnification of 2.77×. Then, combining the estimated back aperture Gaussian beam size with the effective focal length of the objective lens and the immersion index of refraction results in a high NA of 0.44, and a low NA of 0.098 for the system. At these values, the axial FWHM is expected to be 13.6 µm (Supplementary Fig. S7).

Temporal focusing from the DMD could increase the low NA as it disperses light with different wavelengths across the low NA direction at the back aperture of the objective lens. From the grating equation:

$$\lambda = \frac{\Gamma}{M}(\sin\theta_{in} + \sin\theta_{out})$$

where λ is the wavelength, and Γ is the period of grating. For our DMD which is an effective grating with a pitch size of $10.8\ \mu m$ and a diagonal rotation angle,

$$\Gamma = 10.8\ \mu m \times \sqrt{2} = 15.27\ \mu m$$

θ_{in} and θ_{out} are the incident angle and diffraction angle respectively, and M is the diffraction order. For the same incident angle θ_{in} and the same diffraction order M:

$$\frac{\mathrm{d}(\sin\theta_{out})}{d\lambda} = \frac{M}{\Gamma} = \frac{\cos(\theta_{out}) \cdot d(\theta_{out})}{d\lambda}$$

The DMD is positioned such that the diffraction angle θ_{out} is close to 0. With the small angle assumption:

$$\mathrm{d}(\sin\theta_{out}) = \mathrm{d}(\theta_{out}) = \frac{m}{\Gamma} \times d\lambda$$

Considering the FWHM of the bandwidth spectrum of our laser source (Axon-920-2) to be $\Delta\lambda = \sim 13\ nm$, and M = 6, $\theta_{in} = 21.19^{o}$

$$\Delta(\sin\theta_{out}) \approx \frac{6}{10.8\ \mu m \times \sqrt{2}} \times 13\ nm = 0.0051\ rad = 0.29°$$

With an additional 4f system (magnification = 1.2×) between the DMD and the conjugate plane before the tube lens, and the effective focal length of tube lens being 200 mm, the final beam expansion at the objective lens back aperture can be estimated as:

$$\sim 200 \times (0.0051/1.2) = 0.85\ mm$$

Based on the above calculation, our low NA could be increased by ~0.046 to an effective low NA of 0.144. This brings the predicted simulated axial FWHM to be 13.1 µm (Supplementary Fig. S7).

In future implementations, the axial extent of the short line could be reduced by increasing the high NA or increasing the spectrum splitting of the temporal focusing to approach a circular back aperture of 0.44 (in both directions), which has a simulated axial FWHM of 7.9 µm with a much reduced tail intensity, important for volumetric imaging applications.

5. Data acquisition

For a resonant scanner, the angular velocity at the edge of the scan field is highly nonlinear due to the sinusoidal scanning property, and thus, the acquisition at the edge is less preferred. The ratio between the active acquisition time (or spatial trajectory) and the total time (or length) of a line is defined as the fill fraction in temporal domain (or spatial domain) in ScanImage. In the experiment, the fill fraction was 71.3% in the temporal domain and 90% in the spatial domain.

6. Data processing

In the calibration process, we use the pre-trained SUNS algorithm [6] to segment the neurons (i.e., ROIs) in the high-resolution recording. We rejected the ROIs whose temporal traces are in poor signal-to-noise ratio (SNR). This procedure can also be done by manually inspecting the fluorescence traces of each found ROI and identifying the ROIs whose fluorescence trace was noisy and did not show clear calcium transients. For the high-speed recording from the adaptive line-excitation scheme, we first denoised the data through the pre-trained DeepCAD [7, 8], a self-supervised learning algorithm. We then initialized the centroid coordinate of each ROI, based on prior knowledge of the DMD mask and scanning trajectory, in the CaImAn algorithm [9, 10]. This increased the efficiency and efficacy of the algorithm. With CaImAn, the temporal activity traces and the spatial footprints of each individual ROIs could then be extracted.

7. Animal Procedures

All animal experiments and housing procedures were conducted with the approval and guidance from University of California Davis Institutional Animal Care and Use Committee (IACUC). Wild-type C57BL/6J mice (2-5 months old) were injected with AAV1-hSyn-GCaMP6f into the right primary visual cortex, and chronic craniotomy was performed to attach a circular 3.5 mm glass coverslip window for imaging. The coverslip center position was set to be the injection site. A custom stainless steel headplate with a 7 mm hole in the center was attached to the skull surrounding the injection and craniotomy location using dental cement (MetaBond). The coverslip was secured using cyanoacrylate (3M VetBond) and further sealed

with dental cement to cover the exposed bone in the center of the headplate, and to stabilize the headplate for head-fixed imaging. After 3~4 weeks which allows for virus expression, awake imaging was done with the headplate fixed to custom optical posts on top of a 3D printed treadmill on which the mouse was free to run.

References

1. J. N. Stirman, I. T. Smith, M. W. Kudenov, and S. L. Smith, "Wide field-of-view, multi-region, two-photon imaging of neuronal activity in the mammalian brain," Nature Biotechnology **34**, 857-862 (2016).
2. T. A. Pologruto, B. L. Sabatini, and K. Svoboda, "ScanImage: flexible software for operating laser scanning microscopes," Biomed Eng Online **2**, 13 (2003).
3. J.-N. Yih, Y. Y. Hu, Y. D. Sie, L.-C. Cheng, C.-H. Lien, and S.-J. Chen, "Temporal focusing-based multiphoton excitation microscopy via digital micromirror device," Optics Letters **39**, 3134 (2014).
4. T. Chakraborty, B. Chen, S. Daetwyler, B. J. Chang, O. Vanderpoorten, E. Sapoznik, C. F. Kaminski, T. P. J. Knowles, K. M. Dean, and R. Fiolka, "Converting lateral scanning into axial focusing to speed up three-dimensional microscopy," Light Sci Appl **9**, 165 (2020).
5. S. Xiao, W. J. Cunningham, K. Kondabolu, E. Lowet, M. V. Moya, R. A. Mount, C. Ravasio, E. Bortz, D. Shaw, M. N. Economo, X. Han, and J. Mertz, "Large-scale deep tissue voltage imaging with targeted-illumination confocal microscopy," Nat Methods **21**, 1094-1102 (2024).
6. Y. J. Bao, S. Soltanian-Zadeh, S. Farsiu, and Y. Y. Gong, "Segmentation of neurons from fluorescence calcium recordings beyond real time," Nat Mach Intell **3**, 590-600 (2021).
7. X. Y. Li, G. X. Zhang, J. M. Wu, Y. L. Zhang, Z. F. Zhao, X. Lin, H. Qiao, H. Xie, H. Q. Wang, L. Fang, and Q. H. Dai, "Reinforcing neuron extraction and spike inference in calcium imaging using deep self-supervised denoising," Nat Methods **18**, 1395-1400 (2021).
8. X. Y. Li, Y. X. Li, Y. L. Zhou, J. M. Wu, Z. F. Zhao, J. Q. Fan, F. Deng, Z. F. Wu, G. H. Xiao, J. He, Y. L. Zhang, G. X. Zhang, X. W. Hu, X. Y. Chen, Y. Zhang, H. Qiao, H. Xie, Y. L. Li, H. Q. Wang, L. Fang, and Q. H. Dai, "Real-time denoising enables high-sensitivity fluorescence time-lapse imaging beyond the shot-noise limit," Nature Biotechnology **41**, 282-292 (2022).
9. E. A. Pnevmatikakis, D. Soudry, Y. Gao, T. A. Machado, J. Merel, D. Pfau, T. Reardon, Y. Mu, C. Lacefield, W. Yang, M. Ahrens, R. Bruno, T. M. Jessell, D. S. Peterka, R. Yuste, and L. Paninski, "Simultaneous Denoising, Deconvolution, and Demixing of Calcium Imaging Data," Neuron **89**, 285-299 (2016).
10. A. Giovannucci, J. Friedrich, P. Gunn, J. Kalfon, B. L. Brown, S. A. Koay, J. Taxidis, F. Najafi, J. L. Gauthier, P. Zhou, B. S. Khakh, D. W. Tank, D. B. Chklovskii, and E. A. Pnevmatikakis, "CaImAn an open source tool for scalable calcium imaging data analysis," Elife **8**, e38173 (2019).

Supplementary Figures

Supplementary Figure S1.

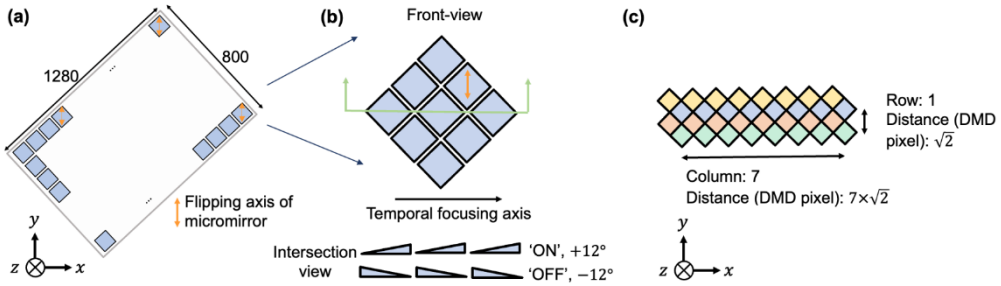

Supplementary Fig. S1. Schematics of DMD layout. (a) The front view of the whole DMD surface and (b) a zoomed-in region: the DMD surface is rotated by 45° so the hinge (i.e. flipping axis) of each micromirror is vertical to the surface of the optical table. The incident light and the diffraction light at the blazed condition are in the horizontal plane parallel with the surface of the optical table. The intersection view shows the tilting conditions of micromirrors at the "ON" and "OFF" states. The line pattern of the incident light is along x direction, and the scanning is along y direction. (c) Adjacent DMD rows which are distinguished by colors. We define the distance between 2 micromirrors in a row as $\sqrt{2}$ pixels.

Supplementary Figure S2.

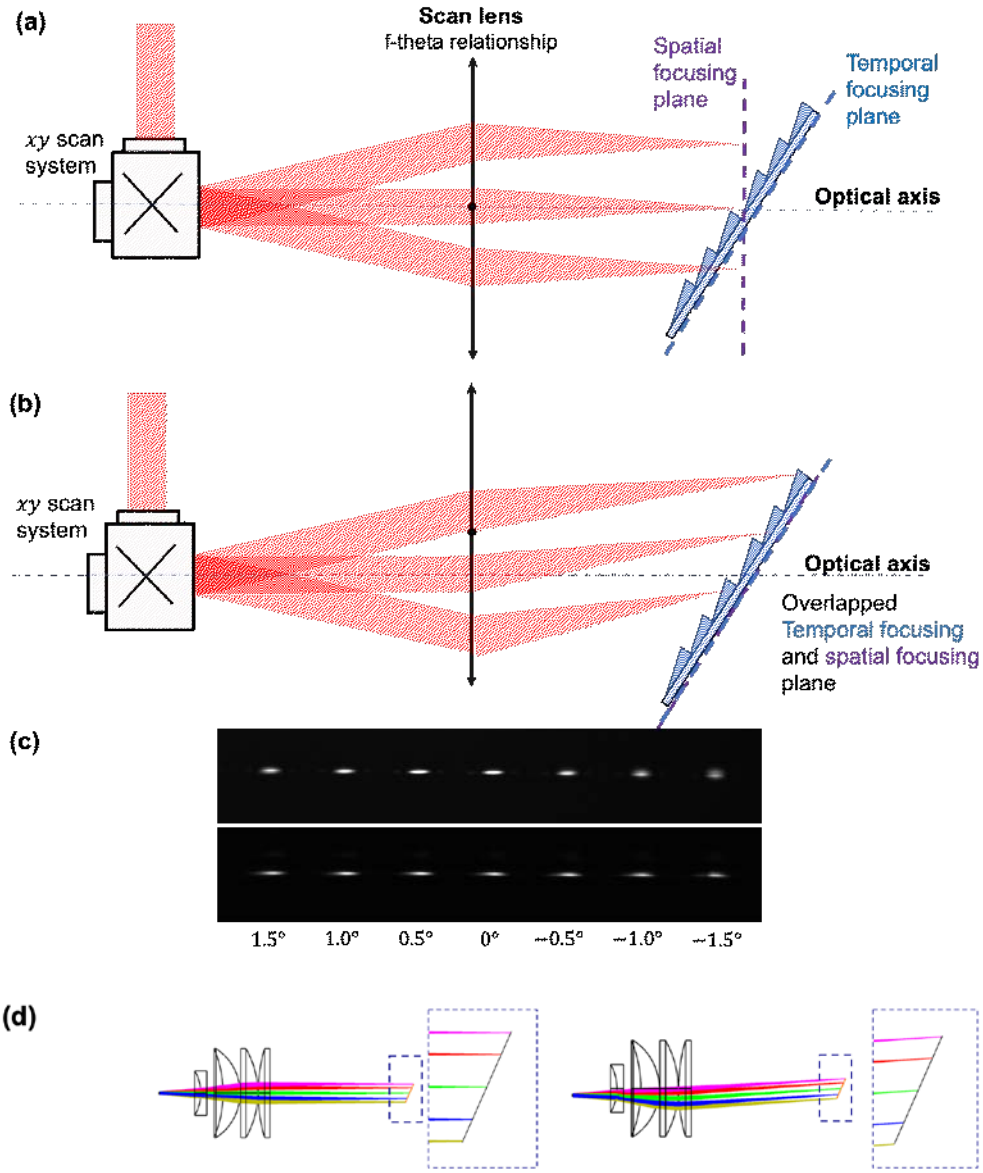

Field (x = 0, y)	Without scan lens offset			With 3.6 mm scan lens offset		
	FWHM y (μm)	FWHM x (μm)	Strehl Ratio	FWHM y (μm)	FWHM x (μm)	Strehl Ratio
-5 deg	30.02	100.80	0.68	33.10	101.2	0.98
-3 deg	36.75	100.70	0.79	33.12	100	0.99
0 deg	35.60	100.58	0.94	33.52	100	0.99
3 deg	37.86	100.68	1.00	34.28	100.2	0.99
5 deg	36.54	100.70	0.98	35.06	100.4	0.98

Supplementary Fig. S2. Illustration of the temporal focusing plane and spatial focusing plane. (a) The conventional scanning scenario: both the scanners and scan lens (SL) are symmetric with respect to the optical axis. Due to the f-theta relationship of the scan lens, the collimating beams from different scanning angles are focused on the plane perpendicular to the optical axis, which is the focal plane of the scan lens. This is different from the temporal focusing plane, which is the DMD surface. (b) With a proper decentered distance between the scanner mirror and the optical axis, the scanning beams from different angles will all spatially focus on the plane of the DMD surface, which has a tilting angle with respect to the focal plane of scan lens. The spatial focusing plane and temporal focusing plane are then overlapped. (c) Experimentally measured focal spots on a conjugate plane of the DMD surface to compare the quality of the focal spot across the field of view (thus different scanning angles of the galvanometer mirror) between the conventional scanning scenario (top) and optimized scanning scenario (bottom). The beam profile has a more consistent shape across the field of view in the optimized scanning scenario. (d) Ray tracing simulation (OpticStudio) of the PSF on DMD plane for a comparison between the conventional scanning scenario (no offset of the scan lens) and the optimized scanning scenario (with offset of the scan lens). A uniform illumination beam passed through a slit in a size of $0.5\ mm \times 1.5\ mm$. The beam (in a shape of a line) was then scanned by a scanner, and passed through the scan lens. The line pattern of the incident light to the DMD is along x direction, and the scanning is along y direction. A detector was placed at the DMD position with a nominal tilting angle of $24°$. The Huygens PSF was simulated for each field (i.e. different scanning angles, indicated by different colors). The table lists the FWHM of the PSF in both directions and the Strehl ratio, which indicates the image quality.

Supplementary Figure S3.

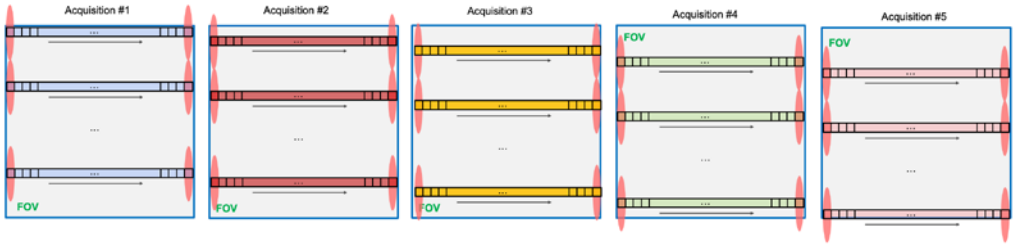

Supplementary Fig. S3. Calibration mode of the two-photon microscope, equivalent to point scanning. The high-resolution image from the equivalent point scanning is constructed from a series of 5 images from single-directional scanning. For each image, 2 lines out of 10 lines on the DMD are set as "ON" state along the single-directional scanning trajectory. The starting point of the FOV scanning is shifted deliberately to ensure the central part of excitation line shape, which has the highest intensity values of the entire line, aligns with those lines set as "ON" states in the DMD. As the DMD is located at the conjugate plane of the image plane and works as an intensity modulator, only one fifth of the area at the sample plane is illuminated. After 5 acquisitions for the 5 DMD masks, 5 PMT images are captured, and the high-resolution image is constructed by sequentially combining the active lines recorded in each image.

Supplementary Figure S4.

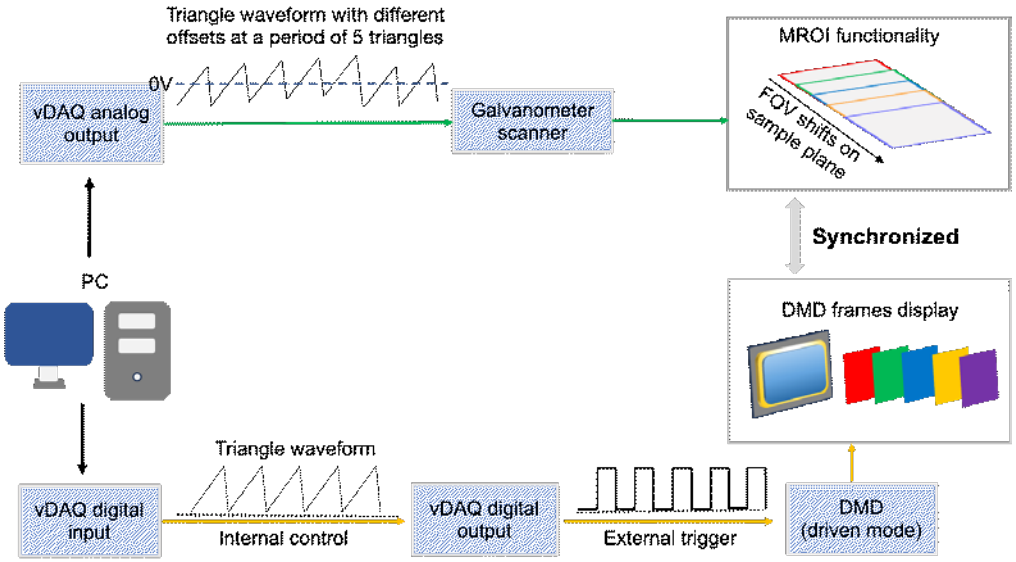

Supplementary Fig. S4. Synchronization and active MROI acquisition. To achieve the equivalent point scanning for a high-resolution image, the simultaneous shifting of the FOV in the galvanometer scanning direction and the change of DMD pattern are required. For each shift of the scanning FOV on the DMD by 2 lines, an offset voltage based on the V/deg parameter for the galvanometer scanner is applied to the command voltage from the vDAQ analog output to the galvanometer scanner. Concurrently, internal communication within vDAQ generates a digital rectangular signal, which is synchronized with the analog output and sent to the DMD portal to update the DMD mask.

Supplementary Figure S5.

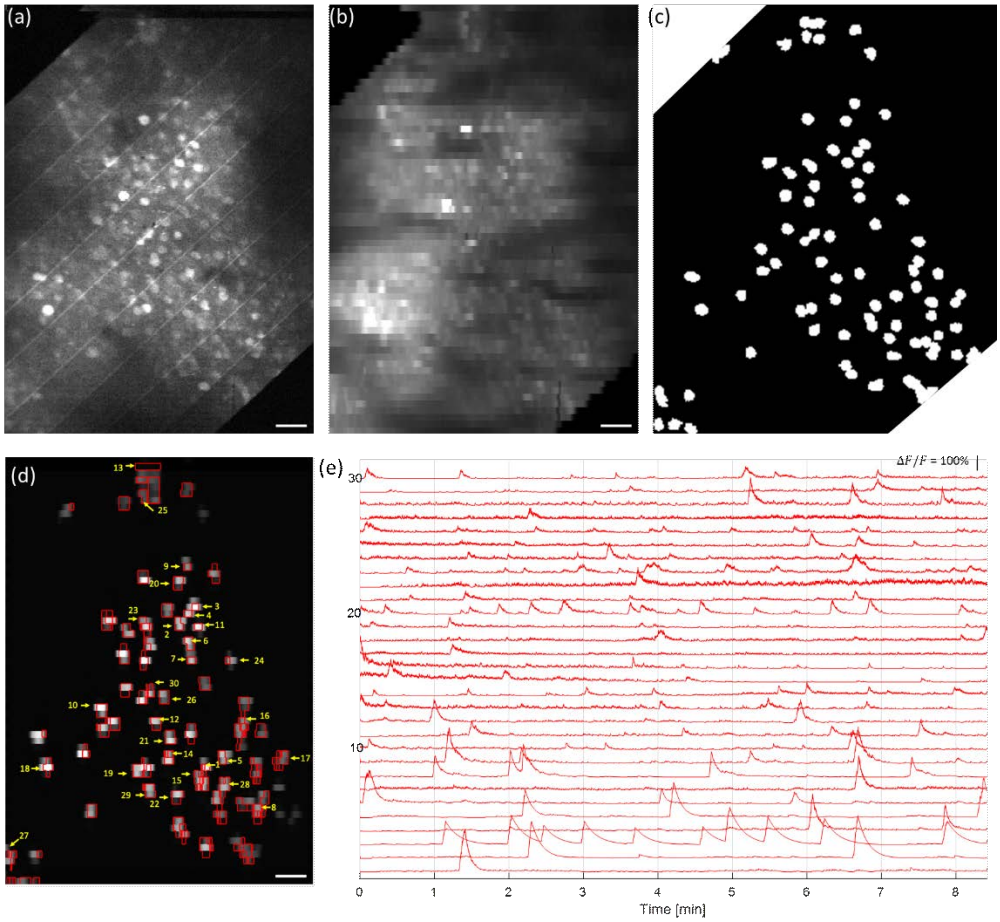

Supplementary Fig. S5. In vivo calcium imaging of mouse V1 at 450 μm depth using the adaptive line-excitation two-photon microscope. (a) Time-series average projection frame of the high-resolution image from the effective point scanning method, which includes the fine contours of the neurons and the background. The image has 256×320 pixels over a 500×695 μm^2 FOV. The periodic lines were artifacts and formed due to the tilted scanning trajectory and corresponding shifted DMD pixels (Supplementary Note 3, Supplementary Fig. S6). They did not impact the segmentation results. (b) Time-series average projection frame of the line-scanning sampled video (256×64 pixels) for the same FOV in (a) without adaptive sampling, where all the pixels in the DMD were turned on. (c) Corresponding binary mask for (a), constructed from the ROI segmentation algorithm of SUNS. Only the neuronal cell bodies with clear neuronal activities within the duration (i.e. ~5 minutes) of the high-resolution video were considered as active ROIs. The DMD mask was cropped from the original 1280×800 image for a better visualization. In our case of adaptive line-excitation, only ~2.9 mW of average laser power was deposited on the brain tissue, which was a significant drop compared to conventional approach without adaptive sampling. (d) Time-series average projection frame of the line-scanning sampled video (256×64 pixels) with adaptive sampling, by applying the mask on DMD. Only the ROIs defined in (c) were illuminated and sampled. The spatial footprints of the extracted ROIs through CalmAn are outlined in red. (e) Temporal activity traces of the representative neurons recorded at 198 Hz, which were indicated by the yellow arrows in (d). The temporal activity traces were extracted by CalmAn. Scale bar in (a)(b)(d): 50 μm.

Supplementary Figure S6.

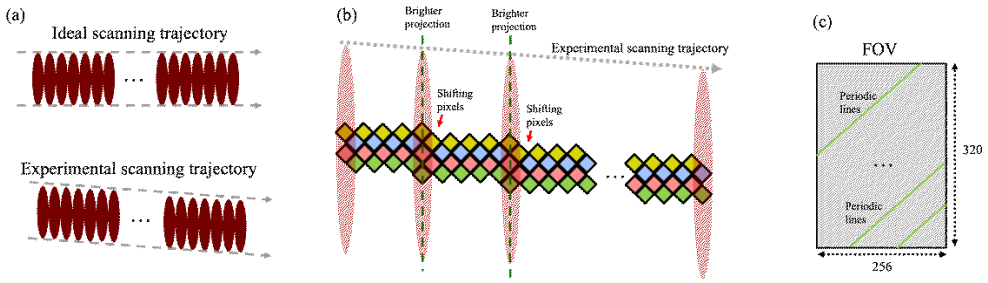

Supplementary Fig. S6. Illustration of the periodic lines in the experimental high-resolution image. (a) Comparison of ideal scanning trajectory and experimental trajectory. (b) Periodic pixels shift along the tilted scanning trajectory. The turned-on pixels on the DMD are shifted periodically to match the exact scanning trajectory in experiment. (c) The resulting periodic lines in the experimental high-resolution image.

Supplementary Figure S7.

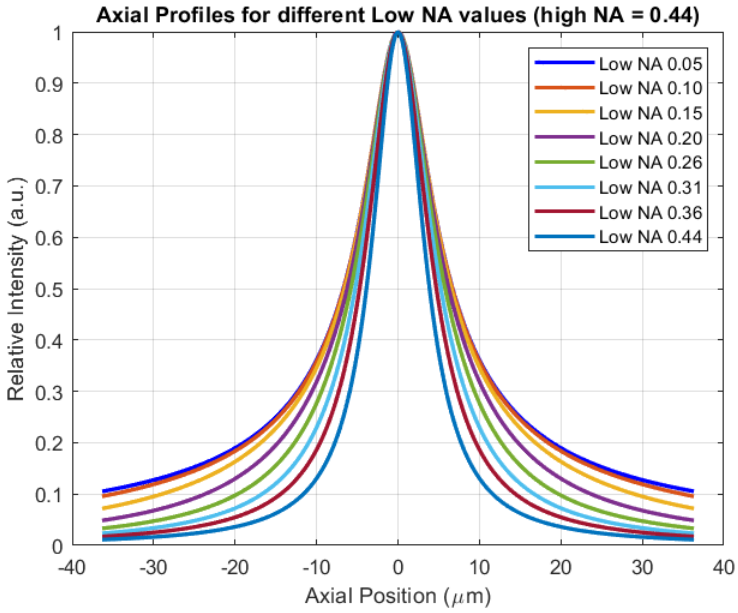

Supplementary Fig. S7. Numerically simulated axial profiles of a line two-photon PSF for a single high NA value with different combinations of low NA values. Simulations were performed using Fourier optics, where a 2D Gaussian beam profile at the back aperture plane of the objective lens was simulated with the desired high and low NA values calculated by using the $1/e^2$ points of the Gaussian back aperture beam in each direction, the focal length of objective and the index of refraction. The beam was propagated to the sample plane via fast Fourier transform (FFT). To get the lateral beam shape at each axial depth so as to obtain the 3D PSF, a Fresnel propagator was repeatedly applied in the Fourier domain (axial step size 0.1-0.5 μm). The resulting 3D PSF was squared to obtain the two-photon PSF. Axial profile was then calculated by summing the X and Y two-photon PSF intensity at each depth.

Supplementary Figure S8.

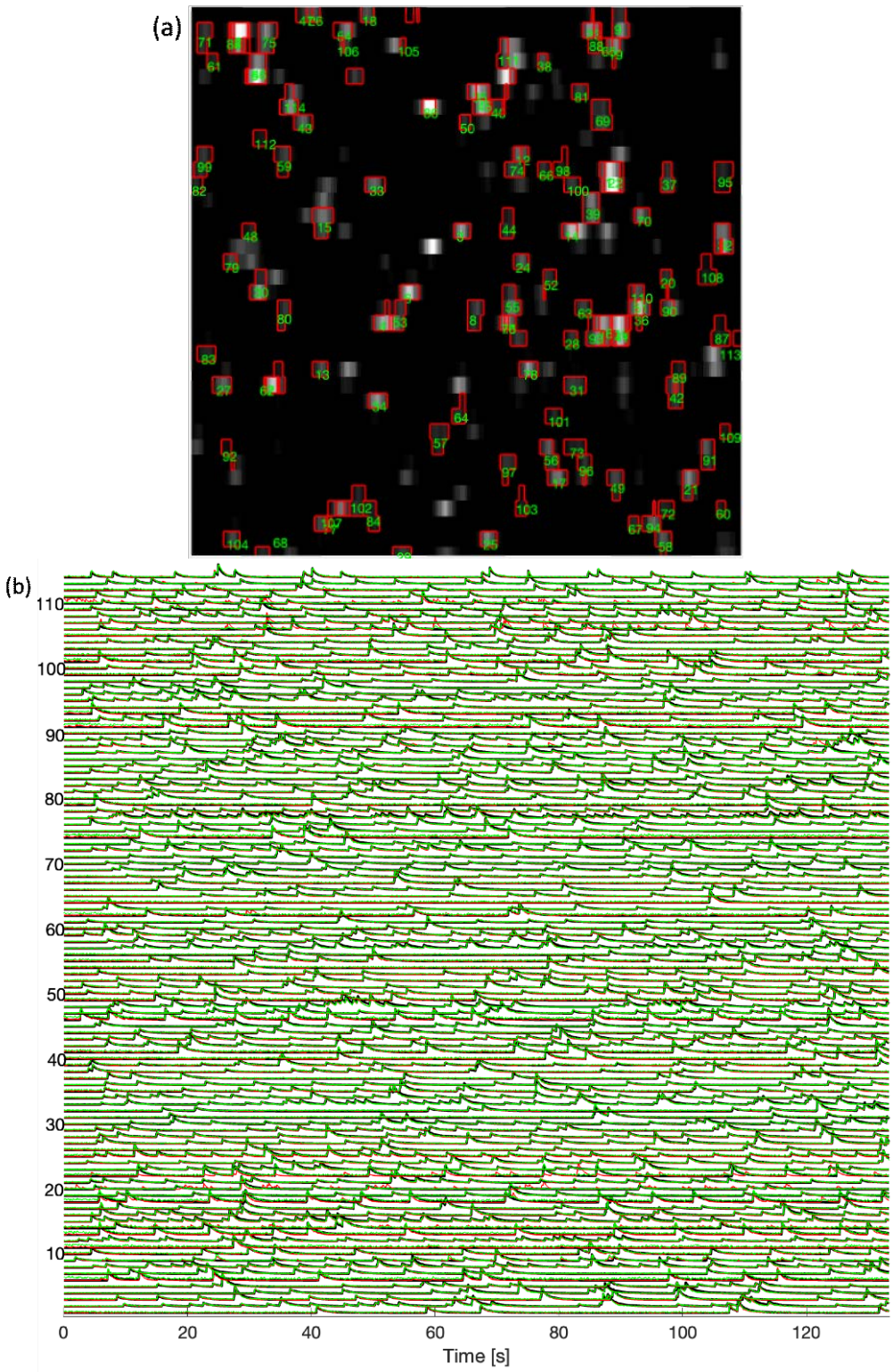

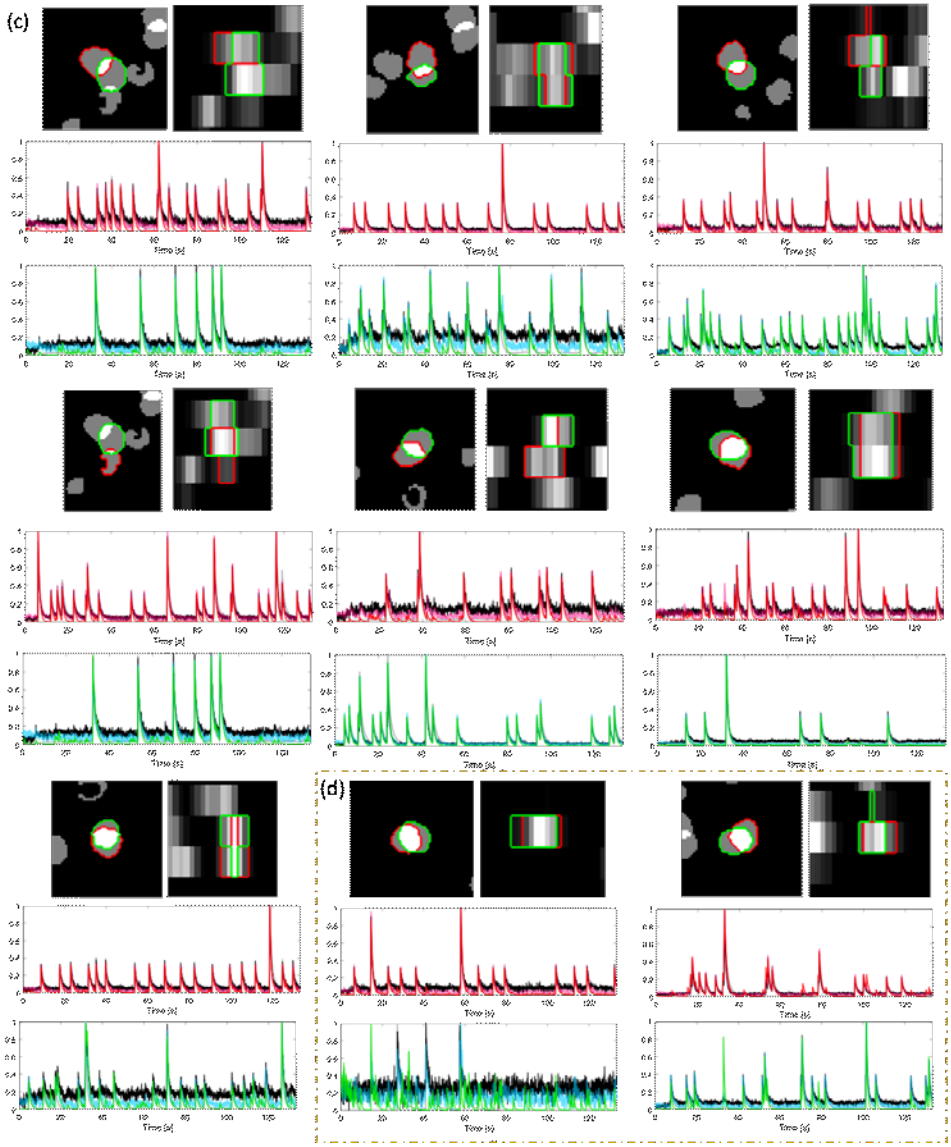

Supplementary Fig. S8. Additional simulation results of the adaptive line-excitation sampling in calcium imaging in Figure 2. (a) The detected ROIs by CaImAn on the adaptive line-excitation sampled video. Only those ROIs with good spatial footprint detection (IoU>0.33) and temporal trace extraction (PCC>0.9) from both high-resolution recording and adaptive line excitation sampled video, against the ground truth, are selected to be plotted here. ROIs are contoured in red and numbered, plotted on the time-series average frame of the video. (b) The normalized temporal activity traces of each ROIs in (a). Black, ground truth with noise and background included; green, extracted traces using CaImAn on the original high-resolution video; red, extracted traces using CaImAn on the adaptive line-excitation sampled video. The high overlap between the green and red traces show that the adaptive line-excitation sampled video preserves the information as the original high-resolution video. (c) Additional representative pairs of comparisons (not shown in Fig. 2(g)) illustrating that the neuronal signals from the neurons with spatial overlaps could be demixed in the adaptive line-excitation sampled video. In each pair group, the top-left and top-right figures show the spatial footprint of the neurons in the high-resolution ground truth and the time-series average projection frame of the adaptive line-excitation sampled video respectively. The middle panel shows the temporal traces of the ROI contoured in red: gray, ground truth without noise and background; black, ground truth with noise and background included; red, CaImAn-extracted from the adaptive line-

excitation sampled video; magenta, CalmAn-extracted from the high-resolution video. Similarly, the bottom panel shows the temporal traces of ROI contoured in green: gray, ground truth without noise and background; black, ground truth with noise and background included; green, CalmAn-extracted from the adaptive line-excitation sampled video; cyan, CalmAn-extracted from the high-resolution video. (d) Two exemplary pairs of spatially overlapped ROIs which were failed to get demixed in temporal signal. This is because their non-overlapped pixels in the adaptive line-excitation sampled video do not have distinctive activities, or their SNRs are too low.